Hearing Research 357 (2018) 10–24

Contents lists available at ScienceDirect

Hearing Research

journal homepage: www.elsevier.com/locate/heares

Research Paper

Quasi-static and dynamic motions of the columellar footplate in ostrich (*Struthio camelus*) measured *ex vivo*

Pieter G.G. Muyshondt [a, *], Raf Claes [b, c], Peter Aerts [b, d], Joris J.J. Dirckx [a]

[a] University of Antwerp, Biophysics and Biomedical Physics, Groenenborgerlaan 171, 2020 Antwerp, Belgium
[b] University of Antwerp, Functional Morphology, Universiteitsplein 1, 2610 Antwerp, Belgium
[c] Free University of Brussels, Department of Mechanical Engineering, Pleinlaan 2, 1050 Brussels, Belgium
[d] University of Ghent, Department of Movement and Sport Science, Watersportlaan 2, 9000 Ghent, Belgium

ARTICLE INFO

Article history:
Received 10 April 2017
Received in revised form
20 October 2017
Accepted 6 November 2017
Available online 9 November 2017

Keywords:
Avian middle ear
Micro-CT
Laser Doppler vibrometry
Digital stroboscopic holography
Finite element modeling

ABSTRACT

The nature of the movement of the columellar footplate (CFP) in birds is still a matter of ongoing debate. Some sources claim that rocking motion is dominant, while others propose a largely piston-like motion. In this study, motions of the CFP are experimentally investigated in the ostrich using a post-mortem approach. For quasi-static loads, micro-CT scans of ostrich heads were made under positive and negative middle-ear pressures of 1 kPa. For dynamic loads, laser Doppler vibrometry was used to measure the velocity on multiple locations of the CFP as a function of excitation frequency from 0.125 to 4 kHz, and digital stroboscopic holography was used to assess the 1D full-field out-of-plane displacement of the CFP at different excitation frequencies. To expose the CFP in the experiments, measurements were made from the medial side of the CFP after opening and draining the inner ear. To determine the influence of the inner-ear load on CFP motions, a finite element model was created of the intact ostrich middle ear with inner-ear load included. For quasi-static loads, the CFP performed largely piston-like motions under positive ME pressure, while under negative ME pressure the difference between piston and rocking motion was smaller. For dynamic loads, the CFP motion was almost completely piston-like for frequencies below 1 kHz. For higher frequencies, the motions became more complicated with an increase of the rocking components, although they never exceeded the piston component. When including the inner-ear load to the model, the rocking components started to increase relative to the piston component when compared to the result of the model with unloaded CFP, but only at high frequencies above 1 kHz. In this frequency range, the motion could no longer be identified as purely piston-like or rocking. As a conclusion, the current results suggest that CFP motion is predominantly piston-like below 1 kHz, while at higher frequencies the motion becomes too complicated to be described as purely piston-like or rocking.

1. Introduction

Up till now, there has been uncertainty about the type of motions that the single ossicle in the middle ear (ME) of birds, the columella, performs under quasi-static and dynamic pressure loads of the tympanic membrane (TM). For dynamic loads, the nature of this motion is crucial as it determines the impedance matching function of the ME and because vibrations of columellar footplate (CFP) form the effective input to the inner ear (IE). For quasi-static loads, the displacements are important since they contribute to ME pressure regulation. Currently, there are two conflicting theories regarding this motion.

The first theory, which was first proposed by Pohlman (1921) based on considerations of ME anatomy in the chicken, describes that rotations of the cartilaginous extracolumella, caused by TM displacements at the tip of the extrastapedial process where the extracolumella attaches to the TM, are converted into piston-like motions at the CFP. According to Pohlman (1921), this conversion takes place by relative rotation of the extracolumella and columella

Abbreviations: (μ)CT, (micro-)computed tomography; CAL, columellar annular ligament; CFP, columellar footplate; FE, finite element; IE, inner ear; LDV, laser Doppler vibrometry; ME, middle ear; SPL, sound pressure level; TM, tympanic membrane

* Corresponding author.
E-mail address: pieter.muyshondt@uantwerpen.be (P.G.G. Muyshondt).

https://doi.org/10.1016/j.heares.2017.11.005
0378-5955/

at the intracolumellar joint, functioning as a hinge. Norberg (1978), on the other hand, explained the origin of piston-like motion as follows: "The intracolumellar joint rotates about the axis of rotation of the extracolumella located at the rim of the TM. The outer end of the shaft of the columella thus moves along the arc of a circle centered at this axis. The spatial relations are such that a line from the extracolumella's axis of rotation to the intracolumellar joint is about normal to the long axis of the extrastapedial process and columella. At small vibrations set up by sound, vibration of the joint then occurs essentially along the line of the axis of the columella. This is the geometry that calls for the least possible deformation of the joint." Also Manley (1990) expressed that the conversion of extrastapedial process rotations to piston-like CFP motions doesn't take place by relative rotation at the intracolumellar joint, but within the flexible extracolumella itself.

The second theory, as proposed by Gaudin (1968), states that the columella doesn't move longitudinally as a piston but rather side-to-side, which goes along with a rocking motion of the CFP rotating around the posterior edge of the oval window. Gaudin (1968) compared this motion of the CFP to "a musician's foot tapping as it rests on the heel". This proposal is based on visual observation of the columella under low-frequency high-pressure stimulation on the TM in samples of different species. According to the author, this movement occurs because of (1) the acute angle between the shaft of the columella and the TM plane, (2) the out-of-center attachment of the columellar shaft to the CFP, and (3) the asymmetrical anatomy of the annular ligament of the columella (CAL) being widest at the anterior edge of the CFP.

Quasi-static and dynamic motions of the columella can be studied by investigating motions of the CFP. In humans and other mammals, motions of the stapedial footplate have been measured extensively using various approaches. In those studies, it was found that the footplate performs mainly piston-like motions at low and middle frequencies, while at higher frequencies the motions become more complicated, including an increase of the rocking components. In birds, out-of-plane CFP motions were measured for the first time in the Barbary dove using Mössbauer spectroscopy (Saunders and Johnstone, 1972). Later, Gummer et al. (1989b) used this technique to examine vibration modes of the CFP in the pigeon by comparing measurements of CFP response obtained under different angles. Their measurements implied the existence of additional vibration modes at higher frequencies alongside the presumed translational vibration mode. In the current study, motions of the CFP are investigated in the common ostrich (*Struthio camelus*). The choice for the ostrich is mainly inspired by the large ear size, which makes it more practical to measure certain mechanical properties of the single-ossicle ear when compared to smaller birds. The anatomy and mechanics of this ear have been examined in previous studies (Frank and Smit, 1976; Saiff, 1981; Starck, 1995; Vallejo Valdezate et al., 2007; Arechvo et al., 2013; Muyshondt et al., 2016b), and it was proposed as a suitable model for total ossicular replacement prostheses in humans (Arechvo et al., 2013). In the present paper, quasi-static motions of the columella are studied with micro-computed tomography (μCT) under static pressure of the MEs. Dynamic motions are investigated with digital stroboscopic holography to determine the full-field 1D out-of-plane displacement map of the CFP, and single-point laser Doppler vibrometry (LDV) is used to determine the 1D frequency response on multiple locations of the CFP with a denser frequency resolution.

It has been shown that the load of the IE can affect footplate displacements in mammals, e.g. in cats (Allen, 1986) and in humans (Hato et al., 2003). The same was observed in one avian species, i.e. the pigeon (Gummer et al., 1989b). For this reason, measurements of footplate motion are usually performed with intact IE via the lateral side of the footplate. Unfortunately, the major surface area of the CFP in birds is inaccessible from outside since the columellar shaft runs through a narrow passage of the ME cavity, behind which the CFP is located. To keep the ME intact, measurements in this study are performed on the CFP from the medial side after opening and draining the IE, as was done on human ears (von Békésy, 1960; Kirikae, 1960). To study the influence of the intact IE on dynamic columellar motions, a 3D finite element (FE) model of the ME is created that includes the IE load of the ostrich (Muyshondt et al., 2016b). The outcome of the model is compared to the experimental results and used to predict CFP vibratory motion in the presence of an intact IE.

2. Materials and methods

2.1. Quasi-static motion

2.1.1. Sample preparation

Five adult ostrich heads (O1 – O5) of animals with ages between 14 and 18 months were obtained from an ostrich farm and stored refrigerated at a temperature of 5 °C in a plastic bag for no more than 5 days before measurement. The ears were not stored frozen and thawed before measurement as this may result in a slightly modified ME response (Ravicz et al., 2000). Before preparing the samples for measurement, the TMs were visually inspected from the side of the external auditory meatus and they were found to be still hydrated. To put the ears under positive and negative static pressure, a custom-made pressure generator was used that was connected to the intracranial air space of the skull via a needle probe (0.8 mm diameter) inserted in the caudal side of the cranium. The intracranial air space forms a complex network of canals and air cells inside a large part of the skull, and is connected to both MEs pneumatically (Larsen et al., 2016). By putting the intracranial air space under a certain pressure, both MEs are put under the same pressure. To prevent tissue dehydration following the sample preparation procedure, the heads were covered with water-soaked paper during one night until right before measurement.

2.1.2. Micro-computed tomography

The ostrich heads were scanned at the University of Ghent's Center for X-ray Tomography (UGCT) using the High Energy CT Optimized for Research (HECTOR) scanner (Masschaele et al., 2013). The pressure generator that was used to maintain a specific pressure in the ears during scanning contains two air pumps (RENA Air 400, Aquarium Pharmaceuticals Inc., Chalfont, PA, USA) which, respectively, generate an over- and underpressure of 4 kPa in two plastic barrels. The barrels have the function of capacitors, suppressing pressure pulses from the pumps. Each barrel is connected to a regulated electromagnetic valve (Valve regulator Type 1093, Bürkert, Ingelfingen, Germany), which can open proportionally to a driving signal. The over- and underpressure delivered by these valves is connected in parallel to the output of the device, and the pressure at this output is measured by a calibrated pressure transducer (SCX01DN, Honeywell, Morris Plains, NJ, USA). A custom-built feedback circuit controls the signal going to the valves so the output pressure is maintained at the preset value. Because the system behaves as a current source, it can maintain this specified pressure level even in the presence of leaks. The pressure generator was located in the same room as the scanner, but it was not put inside the scanner together with the specimen. A flexible tube delivered the pressure from the device to the sample. The tube was flexible enough so it could twist over 360° during scanning without disturbing the specimen. Both ears were included in the

field of view of the detector, so the quasi-static 3D deformation of both MEs could be captured. The MEs were consecutively put under zero static pressure, positive static pressure (+1 kPa) and negative static pressure (−1 kPa) and scans were made for each state. To record the MEs under zero static pressure, the pressure generator was disconnected from the needle probe in the skull. Before each scan, a waiting time of at least 2 min was introduced after putting the sample under pressure, so that any initial displacement or deformation could be released before the start of the scan. The scanner made use of a cone beam with 360° image acquisition and an X-ray tube voltage of 160 kV. The scan time for each scan was 21 min. The image size of the resulting datasets was 997 × 997 × 830 pixels, each with a voxel size of 128 μm.

2.1.3. Image analysis

A semi-automatic image segmentation method was performed in Amira 6.2 (FEI, Hillsboro, OR, USA) to reconstruct the columella, extracolumella and IE from the scans in the different pressure states. To analyze and compare the ME deformation of the three pressure conditions, surface models of the reconstructed structures of the three datasets were realigned such that the surface models of the IE of the three datasets were overlapped the best. The overlapping was performed using a built-in function of Amira based on an iterative closest point algorithm. Subsequently, several components of columellar motion were determined: the displacement of the center point of the CFP u_C (related to piston-like motion of the CFP); the rotational angle of the columella θ (related to rocking motion of the CFP); and the so-called rocking-to-piston ratio r, which is a measure of rocking motion relative to piston-like motion of the CFP (Heiland et al., 1999). Because no in-plane CFP translations were observed with the current resolution of the scans, u_C effectively coincided with the piston component of the CFP (i.e. the component of displacement of the CFP center point in a direction normal to the plane of the CFP). CFP rotations consistently occurred around a single axis close to the anterior-posterior direction. Therefore, the rocking-to-piston ratio for rotations around this axis is defined as

$$r = \left|\frac{u_S - u_I}{2u_C}\right| = \frac{d|\theta|}{2|u_C|}. \quad (1)$$

In this equation, u_S and u_I are the displacement phasors on the edges of the CFP on approximately the superior and inferior side, respectively, d represents the distance between the edges, and θ is the rotational angle around an axis in approximately the anterior-posterior direction. Note that the rotational axis and the axis along which the distance d was measured did not coincide with the long and short axis of the CFP, respectively. θ was calculated based on the rotation of the lateral end of the columellar shaft relative to the CFP center point, which is a valid approach if the shaft of the columella behaves as a rigid body. The absence of deformation in the columella was verified by aligning the reconstructions of the columella in the pressurized state to the corresponding reconstructions in the zero pressure state. Overlapping was performed using the same built-in function of Amira that was used to align the IEs. Visual inspection of the overlapped columellae did not reveal any deformations for the current resolution of the scans.

2.2. Dynamic motion

2.2.1. Experiments

2.2.1.1. Sample preparation. Six additional ostrich heads (O6 − O11) from animals with ages between 14 and 18 months were obtained from an ostrich farm. They were stored frozen at a temperature of −20 °C immediately after death. Prior to measurement, the heads were left to thaw for 16 h at a temperature of 5 °C in a plastic bag. As mentioned, freezing and thawing can slightly change the ME response due to structural changes in the IE (Ravicz et al., 2000). Since the IE was drained for the experiments, this effect could be excluded. To expose the medial surface of the CFP, the caudal side of the head was removed using a bandsaw without damaging the ME structures, and the IE was drilled via the medial wall and drained thoroughly. All ME structures were left intact, including the ME muscles.

2.2.1.2. Laser Doppler vibrometry. The piston-like and rocking motions of the CFP were measured with single-point LDV by measuring the 1D velocity response on different points of the CFP. To achieve this, miniature pieces of reflective foil with a size of 0.4 mm × 0.4 mm and a mass of less than 0.04 mg were positioned on the edges of the long and short axis of the CFP, i.e. on the inferior and superior side for the short axis and on the anterior and posterior side for the long axis. Some manual interpretation was needed to obtain two mutually orthogonal axes that more or less coincided with the longest and shortest edge of the CFP. An additional patch was placed in the center of the CFP on the intersection point of both axes at halfway their length. The mass of each reflective patch is about 1% of the columellar mass (3.88 mg), assuming a mass density and volume of the ossicle as used in the model (see Section 2.2.2). ME vibrations were induced by acoustic stimulation of the TM using a speaker placed at the entrance of the external auditory meatus. In front of the speaker, a pre-calibrated probe-tube microphone (Probe Microphone Type 4182, Bruël & Kjær, Nærum, Denmark) was positioned to record the sound pressure level (SPL). The speaker and microphone were sealed in the external auditory meatus using modeling clay (Otoform Ak, Dreve Otoplastik, Unna, Germany). Stepwise pure-tone sinusoidal signals from 0.125 to 4 kHz, with at least 8 frequencies per octave and a sample rate of 48 kHz, were sent to the speaker through a custom-made amplifier. The range of the frequency sweep corresponded to the auditory range of the emu (Manley et al., 1997), which is the species found in literature most closely related to the ostrich. At the entrance of the external auditory meatus, the SPL was recorded in a first step and corrected to 90 dB SPL for all frequencies in a second step. A LDV system (OFV-534 sensor head and OFV-5000 controller, Polytec, Waldbronn, Germany) that was mounted on a surgical microscope (OPMI Sensera/S7, Carl Zeiss, Jena, Germany) was used to measure the induced vibration velocity of the CFP. The beam of the laser was pointed perpendicularly to the CFP surface (approximated through microscopic view) to measure the out-of-plane motions. The sound and vibration signals were recorded at the same sample rate as the input signal delivered to the speaker. To obtain correct phase information of the stimulation and response signals, phase delays in the setup were taken into account. These delays include the distance between the TM and the microphone at the entrance of the external auditory meatus, and the time delays set by the electronic devices. Signal generation and collection was performed using a 16-bit data acquisition board (USB-6251 BNC, National Instruments, Austin, TX, USA) that was operated in Matlab (Mathworks, Natick, MA, USA). The steady-state magnitude and phase response of the signals at the excitation frequencies were obtained by means of a standard Fourier analysis procedure. The measurements were gathered within 5 min per sample.

2.2.1.3. Digital stroboscopic holography. To obtain direct full-field out-of-plane displacement information of the CFP, digital stroboscopic holography was used to measure the vibrational response of samples O6R and O7L at a selection of stimulus frequencies. The

CFP was coated with a thin layer (~0.1 mm) of white make-up liquid (Aquacolor Soft Cream – White Wet Make-up, Product Code 01129/00, Kryolan, Berlin, Germany) to enhance diffuse light reflectivity. This coating gave the best combination of reflectivity, ease of application and delay of dehydration. The system was again stimulated acoustically via the TM using a speaker positioned at the entrance of the external auditory meatus, in front of which the SPL was recorded with a probe tube microphone (Probe Microphone Type 4182, Bruël & Kjær, Nærum, Denmark). The camera that was used to record the displacement map was positioned perpendicularly to the medial CFP surface to capture the out-of-plane displacements. Displacement maps were recorded for stimulus frequencies from 0.05 to 4 kHz, with 2 frequencies per octave and for sound pressures between 70 and 100 dB SPL. For each stimulus frequency, the displacement magnitude and phase were calculated from the recorded displacement frames at 8 phase instants in one vibration period. More details about digital stroboscopic holography can be found in e.g. Cheng et al. (2010, 2013) and Khaleghi et al. (2013) for a description of the technique, and in De Greef et al. (2014a) for a description of the experimental setup. The measurements were gathered within 5 min per sample.

2.2.2. Finite element modeling

2.2.2.1. Morphology. The geometry of the model is based on the μCT scan of a dissected left ostrich ear (O12L) from an animal that was 18 months old. This ear was also scanned with the HECTOR scanner of the UGCT (Masschaele et al., 2013). To enhance contrast between the different soft tissue structures in the ME, the sample was stained in a daily refreshed 2.5% phosphotungstic acid (PTA) solution in purified water for 48 h before the scan. This solution resulted in the least amount of soft tissue shrinkage in a study of Buytaert et al. (2014), with a linear shrinkage of 3.6%. The scans made use of a cone beam with 360° image acquisition. The image size of the resulting datasets was 1000 × 1000 × 840 pixels with a voxel size of 43 μm. Again, semi-automatic image segmentation was performed in Amira 6.2 (FEI, Hillsboro, OR, USA) to identify the different ME components. The segmented dataset was converted into a surface model built up of triangles. This surface was exported under the STL format that could be imported into FE software (COMSOL Multiphysics 5.2a, Burlington, MA, USA). In Fig. 1, the 3D geometry of the surface model is shown: the structures of the external auditory meatus, ME cavity and IE were excluded from this geometry.

The surface model includes the following structures: the TM that is slightly conical with the tip pointing into the external auditory meatus; the bony columella bounded by the CAL in the oval window; the cartilaginous extracolumella that consists of three arms: the infrastapedial, the extrastapedial and the suprastapedial processes, of which the infrastapedial process ends at periphery of the TM and the extrastapedial process in the conical tip of the TM; a membrane that spans the foramen between the TM and the infrastapedial and extrastapedial processes, which will be called the infrastapedial membrane; the ascending ligament that runs into the middle layer of the TM forming a string of collagenous fibers; and Platner's ligament, which runs from the extracolumella to the otic process of the quadrate at the ME cavity wall. The stapedial and paratubal muscles as described by Starck (1995) were not included in the model. The reason is that, without considering the specific case of muscle contraction, the muscles presumably only influence columellar motion through the boundary conditions of the TM as they are attached to the TM periphery.

2.2.2.2. Model description. The TM was modeled using triangular shell elements. The non-uniform thickness distribution of the TM

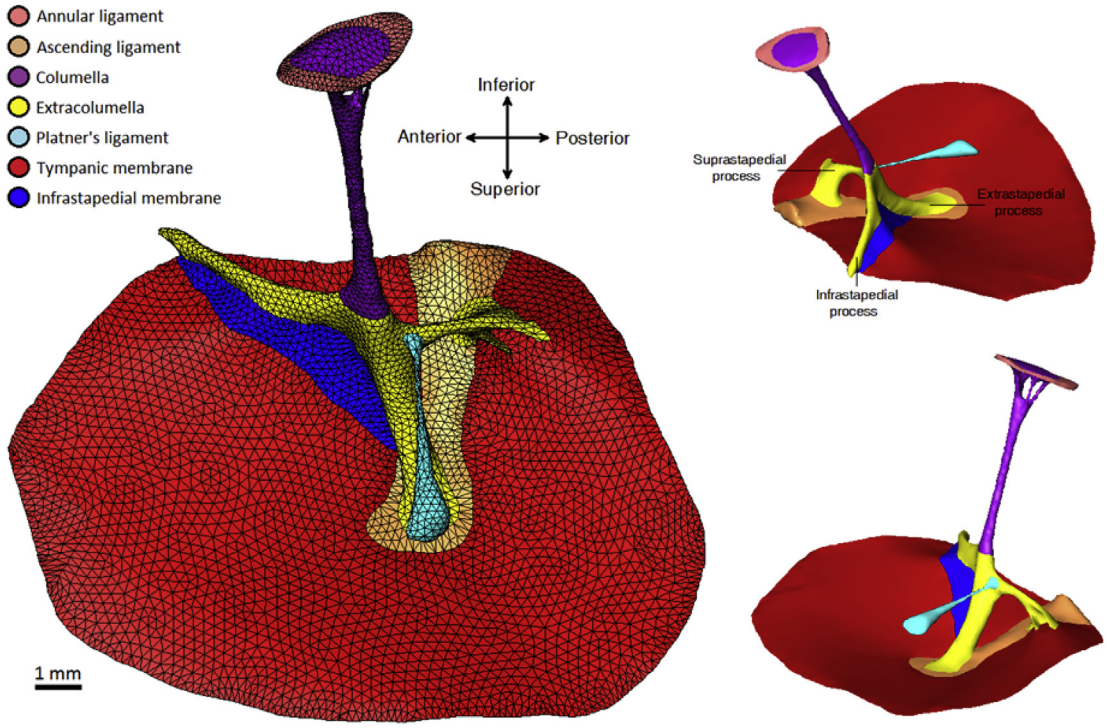

Fig. 1. 3D surface model of the left ostrich ME of specimen O12 used as geometry for the FE model, shown in three different viewing directions. In the left panel, the different components of the ME are shown in the color legend and the anatomical directions are indicated as well. (For interpretation of the references to color in this figure legend, the reader is referred to the web version of this article.)

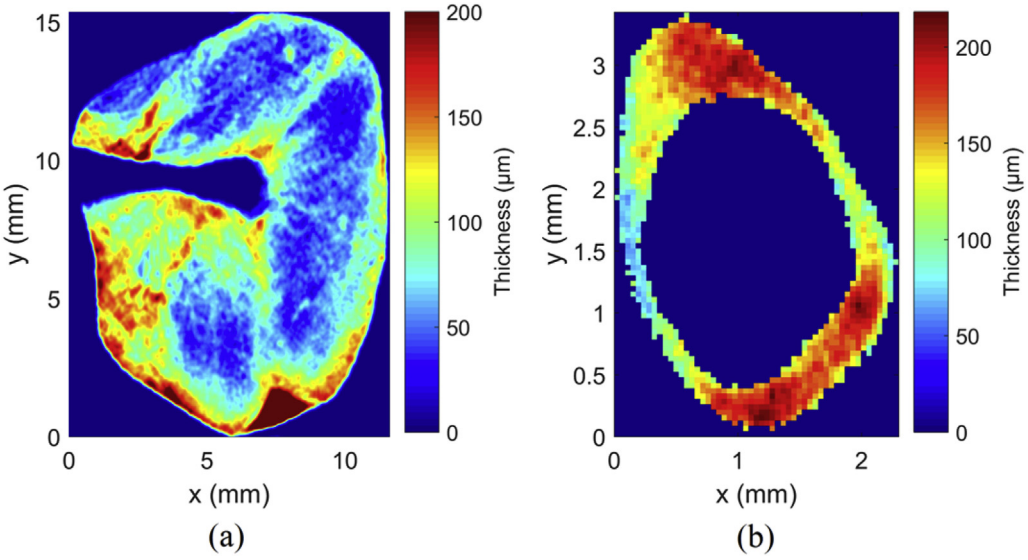

Fig. 2. Smoothed thickness distribution of the left (a) TM and (b) CAL of specimen O12. The thickness distribution of the TM was defined onto the corresponding shell elements of the FE model.

was defined onto the shell elements, and was calculated from the μCT images of the same specimen (O12L) using the shortest distance algorithm described in Van der Jeught et al. (2013). Fig. 2 (a) shows the thickness distribution of the TM, from which the ascending ligament was excluded. In the bottom part of Fig. 2 (a), the thickness map displays an area of increased thickness, which corresponds to the attachment location of the stapedial muscle (Starck, 1995). Note that the thickness in the figure is shown with saturation at 200 μm to make the thickness distribution on the TM more apparent. The maximal thickness near the attachment of the muscle is 607 μm, though it shows as 200 μm in the figure. The thickness distribution of the CAL is shown in Fig. 2 (b). Platner's ligament was modeled using beam elements with a cylinder diameter of 125 μm, taking into account bending and torsion alongside contraction and elongation. All other structures in the geometry were modeled using tetrahedral solid elements. Beams, shells and solids shared translational and rotational degrees of freedom at their respective connections. The intracolumellar joint was modeled as a viscoelastic component on the joined nodes of the columella and extracolumella. This component decouples the motions between both sides of the boundary, which are connected by forces with equal size but opposite direction. The connective forces have an elastic and dissipation component and are defined by $F_C = -F_E = -k(1 + i\eta)(u_C - u_E)$, with F_C and F_E the force vectors on the columella and extracolumella side of the connection, respectively. u_C and u_E are the corresponding displacement vectors, k is the isotropic spring constant of the joint, and η is the damping loss factor.

As boundary condition, Platner's ligament was fully clamped at its outer end. The surface of the CAL boundary was fixed by setting the displacement of its nodes to zero. The periphery of the TM was modeled as hinged instead of fully clamped, since the TM of the ostrich is not directly surrounded by bone but with non-rigid soft tissue (Starck, 1995; Arechvo et al., 2013). Also the outer end of the infrastapedial process was not fixed, as its surrounding tissue allows for movement (Starck, 1995). To incorporate the load of the IE, the complex acoustic IE input impedance Z, as experimentally obtained in the ostrich (Muyshondt et al., 2016b), was imposed on the medial surface of the CFP. Z was modeled as a uniform pressure load p normal to this surface using $p = Z \cdot U$, with U the complex volume velocity of the CFP and CAL in the oval window. This definition is based on the concept that mainly piston-like motion contributes to scala vestibuli pressure, which was shown by Decraemer et al. (2007) and de La Rochefoucauld et al. (2008) in gerbil, following the idea that, in theory, rocking motion does not lead to a net fluid displacement and hence pressure.

The sound stimulus was modeled as a uniform harmonic pressure of 1 Pa (i.e. 94 dB SPL) to the lateral TM surface. Modeling was performed in the frequency domain to study the steady-state response at a series of excitation frequencies. A convergence analysis was performed to determine the mesh size and number of degrees of freedom of the model, which were chosen in such a way that the relative error in the CFP velocity response of two consecutive mesh sizes was smaller than 0.5%.

2.2.2.3. Material properties. Constant, homogenous and isotropic Young's moduli E, Poisson's ratios ν, mass densities ρ and damping loss factors η were used for all structures, as listed in Table 1. Since quantitative information of material properties in the avian ME is largely lacking, parameter values were either estimated, taken from ME models in literature, or adjusted within realistic bounds for the model to match most optimally with experimental data. The TM was modeled using isotropic elasticity parameters instead of an orthotropic description (e.g. Volandri et al., 2011) because preliminary investigations of the elastic fiber distribution of the TM could not detect a regular pattern of arrangement (Starck, 1995). The infrastapedial membrane was given the same parameter values as the TM. The extracolumella is made of hyaline cartilage that may ossify with age, which can drastically increase the stiffness, so the range of possible Young's moduli of the extracolumella is large. A value of 80 MPa gave a good match with experimental data. The ascending ligament is made of collagenous fibers that converge to form a string in the middle layer of the TM. Vallejo Valdezate et al. (2007) described the ligament as solid and tense, which is the basis for the high Young's modulus of 80 MPa that was chosen. The CAL Young's modulus E_{CAL} was calculated

Table 1
Material parameter values used in the FE model, including references for the Young's moduli. References: [a] Herrmann and Liebowitz (1972), [b] Thomassen et al. (2007), [c] Lynch et al. (1982), [d] Muyshondt et al. (2016b), [e] Kirikae (1960), [f] Maftoon et al. (2015), [g] De Greef et al. (2017). E, Young's modulus; ρ, mass density; η, damping loss factor; ν, Poisson's ratio. Parameters without reference were adjusted within realistic bounds for the model to match most optimally with experimental data.

Component	E (MPa)	ρ (10^3 kg/m^3)	η	ν
Columella	14100[a]	2.2[e]	0[g]	0.3[g]
Tympanic membrane	8	1.1[f]	0.2	0.3[g]
Infrastapedial membrane	8	1.1[f]	0.2	0.3[g]
Platner's ligament	21[b]	1.1[f]	0.2	0.3[g]
Annular ligament	0.145[c,d]	1.1[f]	0.2	0.3[g]
Ascending ligament	80	1.1[f]	0.2	0.3[g]
Extracolumella	80	1.1[f]	0.2	0.3[g]

from the ostrich CAL acoustic stiffness impedance $K_{CAL} = 7.05 \cdot 10^{12}$ Pa/m^3 (Muyshondt et al., 2016b) using the expression of the annular ligament compliance subjected to a pure shear stress in Lynch et al. (1982),

$$E_{CAL} = \frac{3wA_{CFP}^2}{tp} K_{CAL}, \tag{2}$$

with $w = 0.39$ mm the average width of the annular space between the CFP and the oval window perimeter, $t = 0.14$ mm the average thickness of the CAL, $p = 8.79$ mm the perimeter of the oval window and A_{CFP} the surface area of the CFP. These geometrical parameters were inferred from the surface model. To compute A_{CFP}, the total surface area of the CFP was projected on the plane normal to the CFP piston axis, yielding a value of $A_{CFP} = 2.82$ mm^2. This value was multiplied with 1.65 to correct for the contribution of the CAL to the net volume velocity in the oval window (Muyshondt et al., 2016b). All structures had the same Poisson's ratio and constant loss factor damping as a function of frequency, except for the columella having zero damping (e.g. De Greef et al., 2014b, 2017). The intracolumellar joint as defined in the current model requires a spring constant to describe its elastic properties instead of a Young's modulus and Poisson's ratio. This constant was chosen isotropic with a value of $2.25 \cdot 10^3$ N/m, which is based on estimations of the Young's modulus of the human incudostapedial joint (0.27 MPa) (Zhang and Gan, 2011; Maftoon et al., 2015) and on the thickness (~60 μm) and surface area (~0.50 mm^2) of the intracolumellar joint. The damping loss factor of the joint was equal to 0.2.

3. Results

3.1. Quasi-static motion

The results of the quasi-static experiments on specimens O1 – O5 are summarized in Table 2. The table contains different components of CFP displacement under either positive or negative ME pressure of 1 kPa: the piston-like displacement u_C, the rotational angle θ and the rocking-to-piston ratio r. The final two rows show the mean and the standard deviation of the mean of each component. In Fig. 3, the deformation of the columellar complex is shown for two illustrative specimens, O1 and O2.

For negative pressure, the CFP undergoes a displacement towards the medial direction as shown in the top panels of Fig. 3. At the same time, the extracolumella undergoes considerable bending in the extrastapedial process. For all samples, except for O2, a transverse displacement at the lateral end of the columellar shaft is observed towards the inferior direction that goes along with a rotation of the CFP, as shown for O1 in the top left panel of Fig. 3. For

Table 2
Components of quasi-static columellar motion in both ears of samples O1 – O5 under positive and negative ME pressure. These components include the piston displacement u_C (mm), the rotational angle around approximately the anterior-posterior axis θ (°) and the rocking-to-piston ratio related to rotations around this axis r. The two bottom rows show the mean $\langle x \rangle$ and the standard deviation of the mean $s_{\langle x \rangle}$ of each component.

Sample	$p_{ME} < 0$			$p_{ME} > 0$		
	u_C (mm)	θ (°)	r	u_C (mm)	θ (°)	r
O1L	0.30	4.9	0.27	0.24	1.0	0.07
O1R	0.30	3.6	0.24	0.27	2.0	0.15
O2L	0.23	0.5	0.04	0.27	2.4	0.16
O2R	0.29	0.7	0.04	0.24	3.1	0.23
O3L	0.20	10.2	0.89	0.37	1.1	0.05
O3R	0.18	7.3	0.67	0.34	1.1	0.05
O4L	0.06	13.9	3.79	0.24	3.0	0.22
O4R	0.07	12.9	3.02	0.27	2.0	0.12
O5L	0.17	9.6	0.89	0.21	0.2	0.02
O5R	0.17	7.7	0.87	0.21	0.3	0.03
$\langle x \rangle$	0.197	7.1	1.07	0.226	1.62	0.110
$s_{\langle x \rangle}$	0.028	1.5	0.41	0.017	0.33	0.025

O2 the situation is slightly different, as extracolumella rotation appears to be converted into a predominantly piston-like CFP motion. Great variation is observed for the rocking-to-piston ratio, with a minimal value of 0.04 for O2, indicating a largely piston-like motion, and a maximal value of 3.79 for O4L, showing a predominantly rocking motion. For all other samples the ratio remains smaller than 1, indicating that the piston component is larger. However, for O3 and O5 a considerable rocking component is present as well.

For positive ME pressure, the 3D displacement of the columella looks similar for all samples. At the lateral end of the columellar shaft, a minor displacement towards the inferior direction is observed that is mostly smaller than for negative ME pressure, which is also noticed when comparing the bottom and top image in the left panel of Fig. 3. Such a motion goes along with a CFP displacement that is larger at the superior than at the inferior side. Rocking-to-piston ratios are smaller for positive than for negative ME pressure (except for O2), with values that are much smaller than 1, showing that CFP motion is mostly piston-like. The out-of-plane displacement is on average larger for positive than for negative ME pressure.

3.2. Dynamic motion

3.2.1. Model validation

First, a convergence analysis was performed on the mesh of the FE model. The total number of degrees of freedom amounts to 187,824. Fig. 4 displays the piston component of the CFP velocity magnitude resulting from the model, both with and without including the IE load. The results are compared to the average of the measurements presented in Arechvo et al. (2013) on 9 individual ostrich ears as reported with intact IE.

The average of the measurements is well represented by the model with IE load. The model matches well with the measurements for the low and mid frequency response up to 1 kHz. The magnitude peak occurs at 0.45 kHz for the model and at 0.47 kHz for the experimental average. The model contains small fluctuations at higher frequencies that are not seen in the mean of the experiments, which presents a smoother curve. However, individual experimental curves contain more variations as a function of frequency comparable to the model. The model stays within the experimental range for most frequencies, only around 1.2, 2.1 and 4 kHz it falls a little outside of this range. The response of the model without IE load has some characteristics different from the model

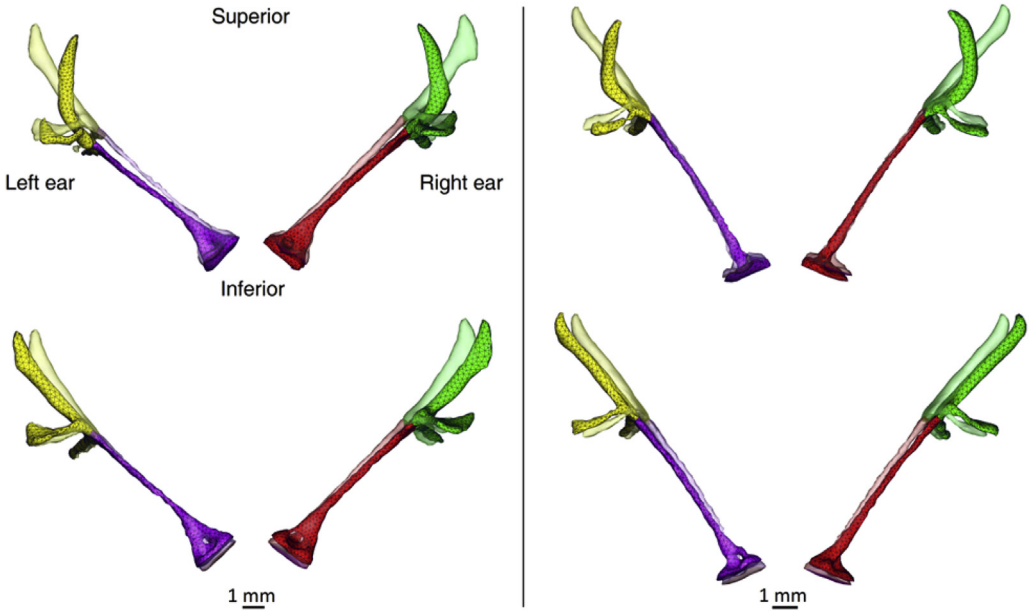

Fig. 3. Posterior view of the quasi-static deformations of the columellar complex under negative (top) and positive (bottom) ME pressure for both ears of specimen O1 (left panel) and O2 (right panel). Transparent surfaces represent the undeformed state (with zero pressure) and opaque surfaces depict the deformed state (with positive or negative pressure). To distinguish the structures of the columella and the extracolumella, they are depicted in different colors. (For interpretation of the references to color in this figure legend, the reader is referred to the web version of this article.)

with IE load, mostly at middle and high frequencies: magnitude values are higher without IE load starting from 0.4 kHz, including a sharper resonance at a frequency of 0.48 kHz.

3.2.2. *Velocity response*

In Fig. 5, the magnitude and phase responses of the CFP velocity are shown for (a) the piston component, (b) the rocking component for rotation around the long CFP axis, and (c) the rocking component for rotation around the short CFP axis. The rocking component for rotation around the long (resp. short) axis is defined as the difference in complex numbers between the two edge velocities of the short (resp. long) axis of the CFP, divided by 2. For rotations around the long (resp. short) axis, the positive direction of rotation is given by the posterior (resp. superior) side of the axis, as opposed to the anterior (resp. inferior) side. CFP responses are displayed for 7 measurement samples obtained with LDV and for the model without and with IE load. From here on, rocking components for rotation around the long and short axis of the CFP will be called long-axis and short-axis components, respectively.

3.2.2.1. Experimental results. For the piston velocity in Fig. 5 (a), we observe that there is considerable variability between different samples, which is also the case for the rocking components. For the piston component, the resonance frequency of the CFP response ranges between 0.34 and 0.62 kHz. The velocity magnitude remains smooth up until 1 kHz. Above this frequency, small and broadly tuned fluctuations become apparent in the decreasing velocity magnitude, and in two samples a second magnitude peak is

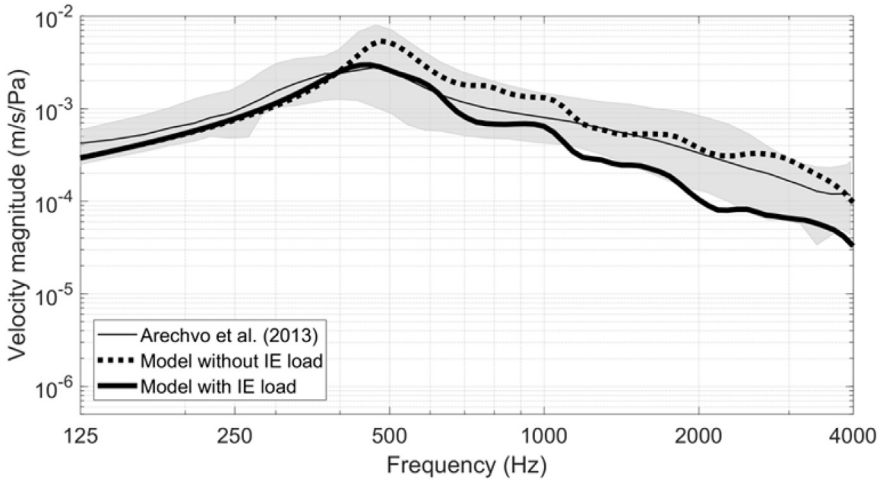

Fig. 4. Piston component of the CFP vibration velocity magnitude (m/s/Pa) as a function of excitation frequency. The thin black line shows the mean of 9 CFP displacement measurements converted to velocity (Arechvo et al., 2013). The grey band represents the measurement range. Bold black lines depict velocity magnitudes of the model with IE intact (solid) and IE drained (dashed).

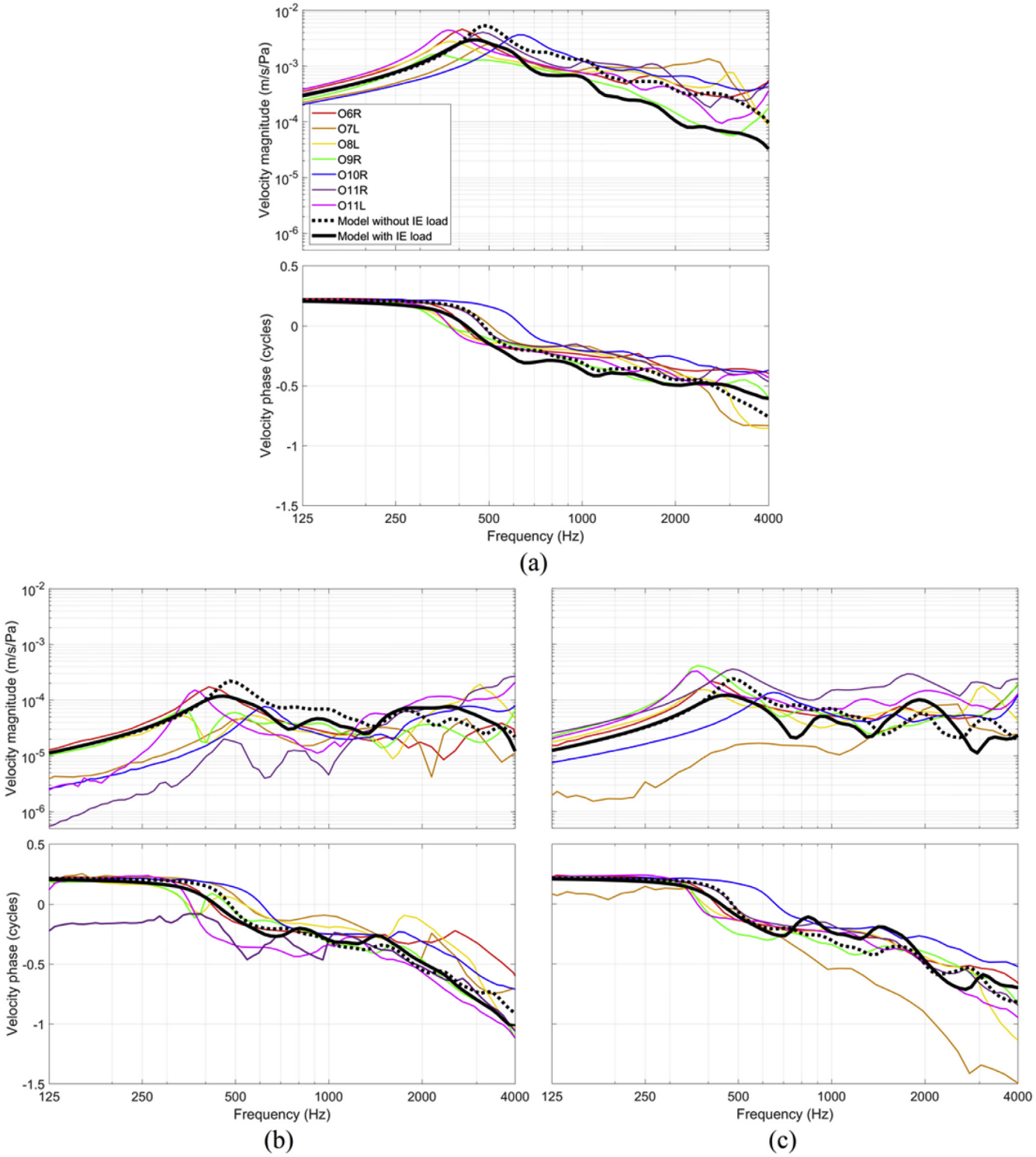

Fig. 5. CFP velocity magnitude (m/s/Pa) and phase (cycles) as a function of frequency for (a) the piston component, (b) the rocking component for rotation around the long CFP axis (i.e. difference between two edge velocities of the short axis divided by 2), and (c) the rocking component for rotation around the short CFP axis (i.e. difference between two edge velocities of the long axis divided by 2). Velocities are shown for 7 LDV measurements with drained IE (colored lines) and for the model without IE load (dashed) and with IE load (solid). Magnitudes are normalized to the stimulation pressure in the ear canal, and phases are taken relative to the phase of the incident pressure.

observed around 3 kHz that goes along with a phase decrease of approximately half a period. For all other samples, the magnitude starts to increase above 3 kHz.

For the long-axis component, as shown in Fig. 5 (b), we observe first of all that the magnitude is 10–100 times smaller than the magnitude of the piston component. We also find that the long-axis component has a resonance at approximately the same frequency as the resonance of the piston component. In two specimens, a dip is observed within the peak of the resonance. Above the resonance frequency, the velocity magnitude decreases as a function of

frequency, but starting from 1 kHz the magnitude begins to fluctuate and increase relative to the piston magnitude. For low and middle frequencies, phases are similar to the phase of the piston component. However, above 1 kHz the phase of the long-axis component decreases faster as a function of frequency, and it contains larger fluctuations than the piston phase. One specimen forms an outlier to the results of long-axis component in the low-frequency range: the magnitude is very low and approaches the noise floor, while the phase differs half a period from the other measurements. However, above 1 kHz the velocity magnitude in this sample increases the most from all specimens, and the phase becomes comparable to the other measurements.

For the short-axis component, as depicted in Fig. 5 (c), we also notice that the magnitude is 10–100 times smaller than the contribution of the piston component. For most samples the low-frequency magnitude is higher than the magnitude of the long-axis component. The short-axis component also contains a resonance peak at a similar frequency as the piston component, and beyond this frequency the magnitude decreases up until 1 kHz. As was found for the long-axis component, the velocity magnitude starts to fluctuate and increase relative to the magnitude of the piston component above 1 kHz, while the phase decreases faster than the phase of the piston component. However, the increase of the magnitude as a function of frequency is more pronounced for the long-axis component. Also for the short-axis component there is one outlier to the results, different from the outlier of the long-axis component. This sample displays a very low magnitude at low frequencies, approaching the noise floor. Also the phase of this sample is lower than for the other measurements, decreasing faster as a function of frequency.

3.2.2.2. Model results. For the model without IE load we notice that the piston component lies within the range of measurements for most frequencies; only around the resonance it exceeds the experimental magnitude range between 0.44 and 0.57 kHz. Nevertheless, the resonance frequency of the model (0.48 kHz) lies within the range of measurements. Above 1 kHz, the model contains small and broadly tuned fluctuations in the decreasing velocity magnitude, which was also noticed for the measurements. The rocking components of the model mostly stay within the experimental range; only the magnitude of the long-axis component exceeds the measurement range between 0.44 and 1.25 kHz, while the magnitude of short-axis component underestimates the measurements between 2.1 and 2.8 kHz. However, the model is qualitatively similar to the experiments; the rocking components are considerably smaller than the piston component, and above 1 kHz they contain larger fluctuations and increase relative to the piston component. At low frequencies, the magnitude of the short-axis component is larger than the magnitude of the long-axis component, but only very little. The phase response of the model is very similar to most measurements.

For the model with IE load, the magnitude of the three velocity components is very similar to the model without IE load up to 0.4 kHz. For higher frequencies the magnitude is smaller with loaded CFP, and around 0.46 kHz the model displays a resonance peak for all velocity components that is smaller and broader than with unloaded CFP. For both rocking components, the model shows a dip in the magnitude around 0.75 and 1.3 kHz that goes along with a small increase of the phase. The short-axis component has an additional magnitude dip near 3 kHz. Around 1.4 kHz, the magnitudes of the rocking components increase above the result of the model without IE load, but around 3.5 and 2.6 kHz they decrease below the unloaded model result for the long-axis and short-axis component, respectively. Phase responses of the model without and with IE load are qualitatively similar. However, the phase decrease of half a period around the resonance evolves more slowly in the model with loaded CFP.

3.2.3. Rocking-to-piston ratio

Fig. 6 displays the CFP rocking-to-piston ratio of the long-axis and short-axis components, for the experiments with drained IE and for the model without and with IE load. For the model without IE load, we computed the effect of adding five mass loads to the CFP, representing the reflective patches, of which the result is also shown in the figure. Ratios were determined by dividing the magnitude of the rocking components by the magnitude of the piston component, which were presented in Fig. 5, for the experiments and models respectively. In Fig. 6, results of the ostrich are compared to the average of measurements in human with IE intact and drained for rotations around the long and short axis of the stapedial footplate (Hato et al., 2003). To quantify the change in CFP response of the specimens over time, for instance due to dehydration, one specimen (O10R) was measured again 15 min after the first measurement. The resulting effect on rocking-to-piston ratios was at the most 3.5 dB for all frequencies, but mostly less than 2 dB (not shown).

3.2.3.1. Experimental results. For the long-axis component, as shown in the top panel of Fig. 6, we observe that there is considerable variability between rocking-to-piston ratios, with a range of about 30 dB, as is the case for the individual velocity components. For low frequencies, the rocking-to-piston ratio mostly remains constant as a function of frequency, though in some samples a local dip or peak is apparent around the resonance frequency. The velocity of the long-axis component is at least 27.5 dB lower than the piston velocity, corresponding to a linear ratio of 0.042. In human, this value is on average −17 dB, or 0.14, for low frequencies with IE intact and drained. There is one outlier to the results, as for the long-axis component in Fig. 5 (b), displaying a very low rocking-to-piston ratio down to −55 dB or 0.0018. Around 1 kHz, the rocking-to-piston ratio starts to increase for most samples, containing small fluctuations. In human, the ratio decreases on average with IE drained, but increases with IE intact. The ratio in ostrich doesn't exceed 0 dB; only one sample reaches a value of 0 dB around 2.8 kHz. At the maximal frequency of 4 kHz, the rocking-to-piston ratio ranges between −24 dB and −4 dB, or 0.063 and 0.63 respectively.

The rocking-to-piston ratio of the short-axis component, depicted in the bottom panel of Fig. 6, also shows considerable variability. At low frequencies, the ratio of the short-axis component remains mostly constant, but values are larger than the ratio of the long-axis component for most specimens. The short-axis component is at least 20 dB lower than the piston component, or a linear ratio of 0.1. In human, rocking-to-piston ratios are higher for rotations around the long axis than for rotations around the short axis at low frequencies. One of the ostrich specimens displays a local peak near the resonance. Another specimen forms an outlier to the rocking-to-piston ratios, as for the short-axis component in Fig. 5 (c), reaching values down to −48 dB or 0.004. The rocking-to-piston ratio of the short-axis component starts to increase around 0.5 kHz, also containing small fluctuations, but the increase evolves much more slowly as a function of frequency than for the ratio of the long-axis component. In human, an increase is observed for the ratio of the short-axis component for both IE intact and drained, but the increase is higher than for the ratio of the long-axis component. Rocking-to-piston ratios of the short-axis component in the current experiments do not exceed 0 dB; although one specimen reaches a value of 0 dB at 4 kHz. The ratio at 4 kHz ranges between −13 dB and 0 dB, or 0.22 and 1 respectively.

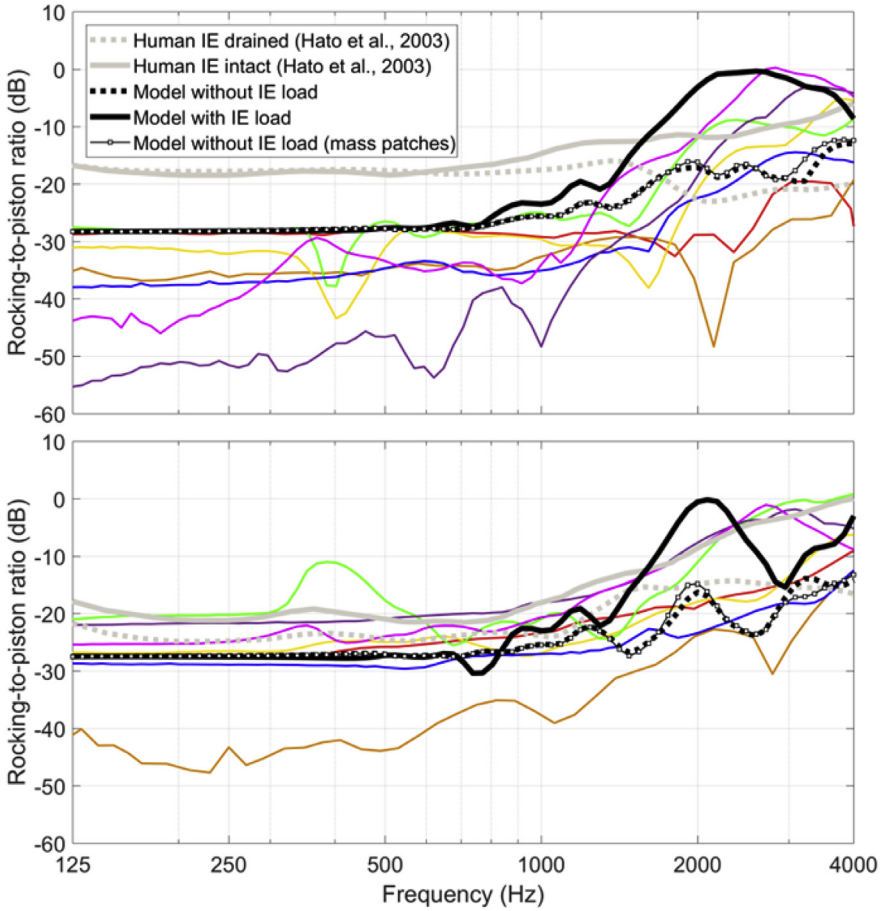

Fig. 6. Components of the CFP rocking-to-piston ratio (dB) for rotations around the long axis (top) and short axis (bottom) as a function of frequency. Ratios are shown for the FE model (bold black lines) without IE load (dashed) and with IE load (solid) and for the LDV measurements (colored lines). Bold grey lines depict the average of human stapedial footplate measurements (Hato et al., 2003) with IE intact (solid) and drained (dashed).

3.2.3.2. Model results. For the model without IE load, we observe that both rocking-to-piston ratios remain constant at low frequencies up until 0.7 kHz. At 0.125 kHz, the rocking-to-piston ratio is equal to −28 dB for the long-axis component and −27 dB for the short-axis component, or a linear ratio of 0.040 and 0.044 respectively. The model stays within the range of measurements in this frequency region; the ratio of the short-axis component of the model approaches the experimental average, while the ratio of the long-axis component almost reaches the upper bound of the experiments. Starting from 0.7 kHz, both ratios of the rocking components start to show an overall increase as a function of frequency up to 4 kHz, and the fluctuations are larger than in the experiments. At 4 kHz, maximal rocking-to-piston ratios of −13 dB (or 0.22) and −14 dB (or 0.20) are reached for the long-axis and short-axis component, respectively. Adding five point masses of 0.04 mg to the CFP surface in the model, representing the reflective patches, has minor influence on the results as shown in Fig. 6.

For the model with IE load, both ratios are the same as without IE load for frequencies below 0.6 kHz. For measurements in human, the rocking-to-piston ratio of the short-axis component is 4 dB higher with intact than with drained IE at low frequencies. Above 0.8 kHz, the ratios of the model with loaded CFP start to increase relative to the condition with unloaded CFP, reaching a maximum of 0 dB between 2 and 3 kHz, so that CFP motion can no longer be identified as purely piston-like or rocking. Beyond the maximum, the ratio of the long-axis component for the model with IE load decreases slowly down to −9 dB or 0.35 towards 4 kHz. For the short-axis component the decrease is much larger (down to −15 dB or 0.18), but towards 4 kHz the ratio rises again up to −3 dB or 0.71. For the average of measurements in human, such a decrease is also observed beyond 6 kHz (not shown). Beyond 3 kHz, rocking-to-piston ratios of the model with loaded CFP again increase above the model result with unloaded CFP, reaching values of about −5 dB or 0.56.

3.2.4. Full-field displacement

Fig. 7 shows the full-field 1D out-of-plane displacement magnitude and phase of the CFP, for the digital stroboscopic holography experiments measured in O6R and O7L with IE drained, and for the model without and with IE load. Displacement maps are shown for 3 selected frequencies of 0.2, 0.8 and 3.2 kHz.

3.2.4.1. Experimental results. At 0.2 kHz, the magnitude and phase maps are almost entirely uniform for both specimens, corresponding to a piston-like motion. At 0.8 kHz, the displacements in O6R are a little larger at the posterior and inferior side of the CFP compared to the anterior and superior side. In O7L the displacement is neither uniform, but the largest displacement occurs on a different part of the CFP, i.e. at the posterior and superior side. For both specimens, the phase maps remain uniform. This behavior indicates a small increase of the rocking components, although the piston component remains clearly dominant. At 3.2 kHz, the rocking components appear to increase further relative to the piston

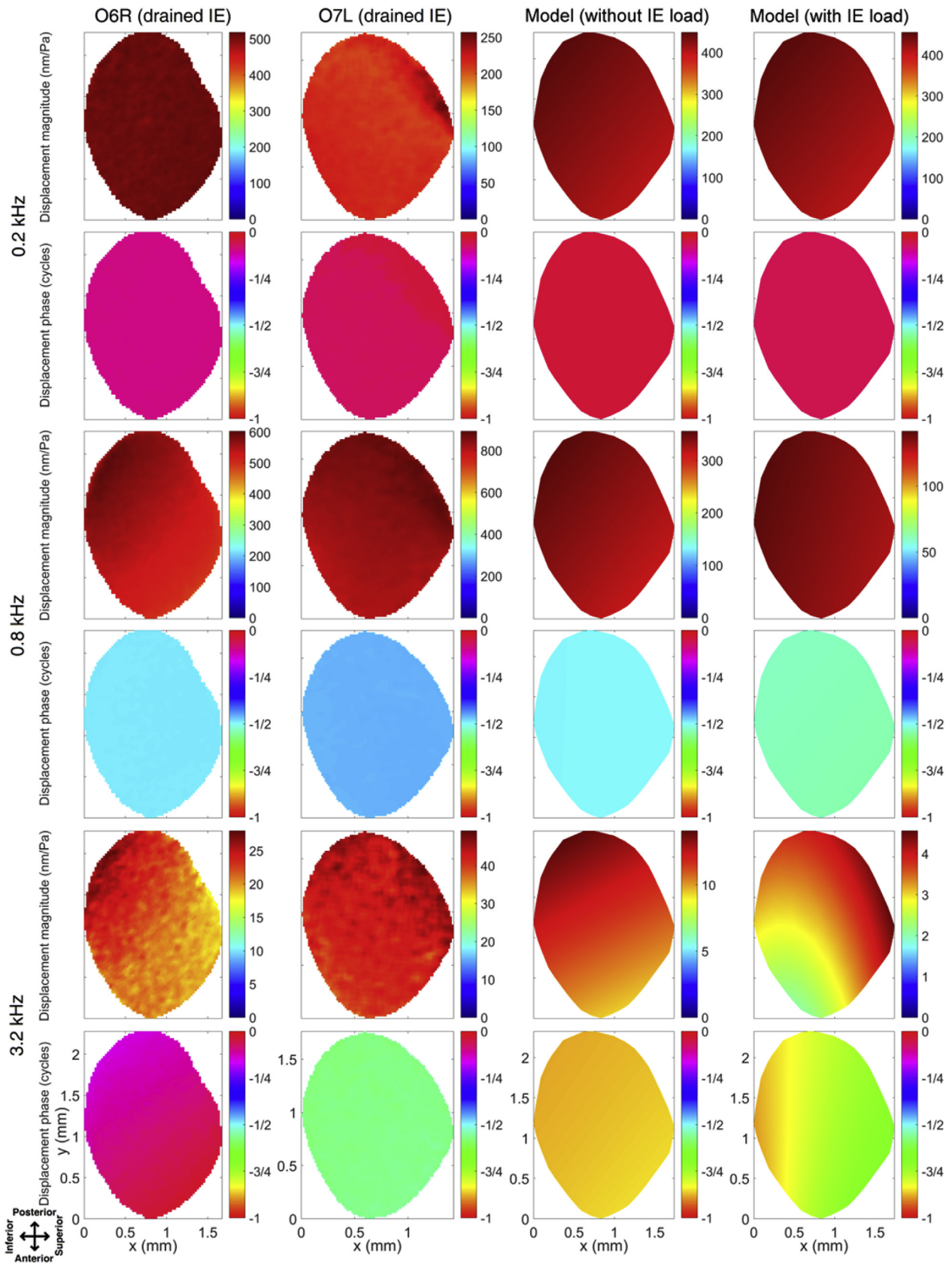

Fig. 7. Full-field 1D out-of-plane displacement magnitude (nm/Pa) and phase (cycles) for 3 selected frequencies of 0.2, 0.8 and 3.2 kHz. Magnitudes are normalized to the stimulation pressure in the ear canal. The first two columns depict experimentally obtained displacement maps measured with digital stroboscopic holography in specimen O6R (mirrored) and O7L with IE drained. Experimental phase maps have arbitrary reference value. The last two columns show displacement maps of the model without and with IE load. For the models, phases are taken relative to the phase of the stimulation pressure. Approximate anatomical directions are indicated in the bottom-left part of the figure.

component in O6R, since displacements on the posterior and inferior edges of the CFP are almost twice as large as on the anterior and superior edges. Also, the phase map is no longer completely uniform in this sample. In O7L, however, the displacement maps at 3.2 kHz are qualitatively similar to the maps at 0.8 kHz.

3.2.4.2. Model results. At 0.2 kHz, the displacement map is almost completely uniform for both the model without and with IE load. Also at 0.8 kHz, the displacement maps of the models remain largely uniform. Only at 3.2 kHz the behavior starts to change: as in O6R, the magnitude map of the model without IE load contains larger displacements in the inferior and posterior regions of the CFP, but the phase remains uniform. For the model with IE load a clear rocking component emerges and the phase is no longer uniform. Still, the piston component remains the largest at this frequency, as can be deduced from Fig. 6. However, the overall dynamic motion of the columella in the model is too complicated to be described as purely piston-like or rocking. Adding a mass load of the coating to the CFP surface in the model, using a layer thickness of 0.1 mm and a mass density of 1000 kg/m^3, has only minor effect on CFP displacements (not shown).

4. Discussion

4.1. Quasi-static motion

4.1.1. Experiments in literature

In the past, deformations of the columellar complex under the influence of quasi-static pressures have been measured in several bird species. Nevertheless, quantitative results of rocking relative to piston-like motion are lacking.

Gaudin (1968) made photographs of columellar displacement under low-frequency high-pressure simulation of the TM in different species, by applying pressures in the external auditory meatus. The observed columellar displacements were side-to-side, perpendicular to the columellar shaft, and CFP displacements occurred mostly at the anterior edge of the oval window.

Mills and Zhang (2006) observed columellar displacements under static pressures of +1 and −1 kPa applied in the external auditory meatus of different birds, and found a tilting of the extracolumella and a flexion of the intracolumellar joint, which produced a rocking motion of the CFP around its anterior edge rather than a direct displacement into the scala vestibuli. Later, Mills et al. (2007) performed similar pressure experiments in the ear of the common guillemot, measuring CFP displacements of 100 μm at a positive pressure of 2 kPa in the external auditory meatus. No pronounced rocking motion of the CFP was observed.

Arechvo et al. (2013) measured displacements at the center point of the CFP in the ostrich as a function of positive input pressure applied in the external auditory meatus from 0 to 2 kPa. The average CFP displacement was equal to 270 μm at 1 kPa and 330 μm at 2 kPa. When a positive or negative pressure was applied to the external auditory meatus, considerable bending occurred in the extrastapedial process of the cartilaginous extracolumella, while Platner's ligament limited displacements of the CFP in and out of the oval window.

Thomassen et al. (2007) created a 3D FE model of the static displacements of the columellar complex in the cave swiftlet and 2D models of several other avian species. The 3D model of the cave swiftlet resulted in rocking motions of the CFP, behaving as a tapping foot as described by Gaudin (1968). The CFP displacements inferred from the 2D models were either rocking or piston-like in nature, depending on the ME geometry of the species.

4.1.2. Experimental results

In the current study, quasi-static columellar displacements in both ears of the ostrich were induced simultaneously by applying a positive or negative pressure of 1 kPa inside the intracranial airspace. Applying pressures via the inside or the outside of the ME doesn't result in different columellar displacements, as only the pressure gradient over the TM is determinative for ME deformations. Piston-like and rocking motions of the CFP for both pressurized conditions were quantified by comparing μCT scans of the head with and without pressure.

Based on the results we could conclude that, for positive ME pressure, CFP motion was predominantly piston-like with only a small rocking component. For negative ME pressure, the rocking-to-piston ratio was larger than for positive ME pressure, except for specimen O2, but the piston component was still larger than the rocking component. Only for sample O4 rocking motion was dominant. For two other specimens (O3 and O5) a considerable rocking component was present as well. The deviating result of O2 may be related to a different geometry of the columellar complex, as can be deduced from Fig. 3: in O1 the undeformed extrastapedial process has a curved shape with its distal end located medially to the elongated long axis of the columella, while in O2 the distal end of the curved extrastapedial process is located laterally to this imaginary axis, possibly leading to a different CFP motion. The large rocking motion observed in O4 for negative ME pressure, on the other hand, goes along with a large rotation of the extrastapedial process (i.e. a rotation caused by medial displacement of the distal part of the process) that leads to an almost straight angle between the long axes of the extrastapedial process and the columella (not shown). Such a motion is associated with considerable buckling at the intracolumellar joint, but the behavior of the outlier may also represent a damaged ear. Displacements at the distal end of the columellar shaft that are transverse to the long axis of the shaft are an indication of rocking motion. However, since the columellar shaft of the ostrich is very long relative to the size of the CFP, the encountered transverse motions involve only small CFP rotations as observed in most samples. Therefore, the rocking component remains small compared to the piston component in most cases, which is mostly in agreement with the observation of Mills et al. (2007) reporting piston-like behavior, and different from Gaudin (1968) and Mills and Zhang (2006) who reported rocking motion. Out-of-plane CFP displacements were on average 0.226 mm for positive and 0.197 mm for negative ME pressure. The latter result is considerably smaller than the 0.27 mm observed by Arechvo et al. (2013). The observation that piston-like motion is smaller for negative than for positive ME pressure may indicate the presence of a protective mechanism that minimizes excessive displacement of the CFP into the scala vestibuli, as proposed by Mills and Zhang (2006). The protective mechanism may reduce piston-like motion by partially converting it into rocking motion, which does not involve a net displacement into the scala vestibuli.

Rocking-to-piston ratios resulting from the quasi-static experiments, especially for negative ME pressure, were generally larger than the ratios obtained with the dynamic measurements at the lowest measured frequencies, which are discussed in the following section. This discrepancy is probably due to nonlinearity of the quasi-static CFP displacements: at the applied static pressures of 1 kPa, CFP displacements become nonlinear (Arechvo et al., 2013), which differs from the dynamic CFP motions that remain well within the linear response regime at the stimulus pressure of 1 Pa. Nonlinearities may involve material nonlinearities of the columellar complex, but also geometric nonlinearities or nonlinearity of the IE load. In case of a geometric nonlinearity, the physics equations can no longer be formulated with respect to the object's undeformed state, but they depend on the effective deformation

when becoming large. The conical shape of the TM in the lateral direction could produce such nonlinearity: if the TM deforms in the lateral direction it may stretch and gain tension, while a medial deformation may lead to a loss in tension. At high quasi-static pressures these nonlinearities may lead to asymmetry in CFP displacement between positive and negative pressure, as was found for the rocking-to-piston ratios listed in Table 2.

4.2. Dynamic motion

4.2.1. Experiments in literature

In mammals, motions of the stapedial footplate have been measured and quantified extensively in different species, using various approaches. These species include human (e.g. von Békésy, 1960; Kirikae, 1960; Heiland et al., 1999; Huber et al., 2001; Hato et al., 2003; Sim et al., 2010), cat (Guinan and Peake, 1967; Decraemer et al., 2000), gerbil (Decraemer et al., 2007; Ravicz et al., 2008) and guinea pig (Eiber et al., 2007, 2012; Huber et al., 2008). The latter three used mechanical stimulation instead of acoustic stimulation to generate rocking motions on the footplate.

Full-field dynamic motions of the CFP in the single-ossicle ear have only been measured qualitatively in one reptile species, the alligator lizard (Rosowski et al., 1985), by using stroboscopic illumination with high stimulus levels (Guinan and Peake, 1967). The columella was shown to vibrate mostly as a piston.

In birds, Saunders and Johnstone (1972) measured CFP vibrations in the Barbary dove using Mössbauer spectroscopy. Gummer et al. (1989a) used the same technique to measure CFP responses in anesthetized pigeons along several axes. CFP vibrations were measured with IE intact, fenestrated and drained. The authors found a frequency dependence of the phase response on the spatial angle of the measurement axis. This frequency dependence provided direct evidence for vibration modes additional to the presumed piston-like mode. For high frequencies above 2 kHz, sharp and broadly tuned antiresonances were observed in the CFP response with IE intact, involving amplitude notches, large phase drops up to 2 cycles and positive phase slopes.

More recently, Arechvo et al. (2013) measured the out-of-plane CFP displacement magnitude response in the ostrich with intact IE using LDV (Fig. 4). Results of that study are similar to our measurements, with a resonance peak near 0.5 kHz. Our results show slightly higher magnitudes at high frequencies, which was probably due to draining the IE. LDV was also used to measure the extrastapedial tip and CFP response in the mallard (Muyshondt et al., 2016a). Extrastapedial tip vibrations were measured with IE intact and drained, and CFP vibrations with IE drained. After draining the IE, the extrastapedial tip response mainly changed in the middle and high frequency range, and the resonance peak shifted to higher frequencies. To determine the impedance of the IE in ostrich, the columellar response was measured by Muyshondt et al. (2016b) with IE intact and IE drained under magnetic stimulation of the ossicle. Again, removing the IE fluids mainly influenced the response in the middle and high frequency range, and the resonance peak was shifted to higher frequencies.

4.2.2. Experimental results

In the current study, dynamic motions of the CFP were measured with LDV and digital stroboscopic holography in the ostrich after draining the IE. The measured specimens showed a large quantitative variation in the CFP velocity response, which was also the case for the rocking-to-piston ratios. Also in humans, large differences between samples were observed in motions of the stapedial footplate (Sim et al., 2010), which were presumed to be due to individual differences in ME anatomy. However, differences in vibration response may also indicate differences in material properties. Specific features to some specimens, such as dips in the response near the resonance frequency or outliers in magnitude and phase, may reflect small changes or differences in physiological condition. Qualitatively, the results of CFP motion were similar and the samples exhibited largely piston-like behavior at low frequencies below 1 kHz. Towards higher frequencies, the rocking components increased as a function of frequency, although never exceeding the piston component.

In many aspects, the results are qualitatively similar to what was found in the aforementioned experiments on mammalian ears. In Hato et al. (2003), stapedial footplate motions were measured in human from 0.1 to 10 kHz before and after draining the IE. With intact cochlea, the average footplate motion was piston-like below 1 kHz. Above 1 kHz, rocking motions for rotations around the long and short axes of the footplate started to increase, and around 4 kHz they became most dominant, reaching a peak at 6 kHz. With cochlea drained, the piston component increased for all frequencies, while the rocking components slightly increased for low frequencies and decreased for high frequencies. Due to the increase of the piston component after drainage, rocking-to-piston ratios decreased overall, leading to a predominant piston-like motion for all frequencies, which is in agreement with the presented ostrich measurements with IE drained.

4.2.3. Model results

To study the influence of the IE on displacements of the CFP, a FE model was constructed of the ME with an IE load model that is based on the net volume velocity and uniform pressure of the IE fluid on the medial CFP surface. As rocking motion does normally not lead to a net fluid displacement, the pressures and velocities in this model are supposedly caused by piston-like motion. As a consequence, the load will mainly affect the piston component, as can be noticed in Fig. 5. Nevertheless, rocking motions have been shown to contribute to cochlear activation by changes in the compound action potential of the cochlea (Eiber et al., 2007, 2012; Huber et al., 2008). However, the activation threshold was higher and the sensitivity lower for the rocking components than the corresponding values of the piston component. A cochlear model of Edom et al. (2013) showed that rocking motion contributed to basilar membrane motion, but under normal conditions the piston component was dominant; while piston-like motion leads to a pressure wave that travels across the basilar membrane, rocking motion causes only a weak pressure wave compared to the pressure right behind the footplate. Decraemer et al. (2007) and de La Rochefoucauld et al. (2008) found no clear indication that rocking motion leads to pressure behind the footplate, so despite that vestibular pressure caused by rocking motion is certainly present, its magnitude must be small compared to the corresponding values of the piston component. As such, the impedance of piston-like motion must be influenced more by the status of the cochlea than the impedance of rocking motion, as suggested by Hato et al. (2003). Presumably, introducing a small load to the model related to rocking motion will slightly reduce the magnitude of rocking motion. In this sense, the current model with an IE load based on the net volume velocity and uniform pressure poses an upper bound on the effective rocking-to-ratios with intact IE.

For the model without IE load, we observed that the rocking-to-piston ratios belonging to rotations around both the long and short CFP axis remained constant as a function of frequency up to 0.7 kHz, which was similar to most measurements. At higher frequencies, the rocking-to-piston ratios exhibited an overall increase as a function of frequency, containing evident fluctuations. When comparing the CFP motion of the model with and without IE load, it was found that the frequency response of the piston component

mainly changed at middle and high frequencies, as observed experimentally in different birds (Gummer et al., 1989b; Muyshondt et al., 2016a,b).

When the IE load was included, the rocking components started to increase at 0.8 kHz relative to the situation with unloaded CFP. Around 2–3 kHz, rocking-to-piston ratios showed that CFP motion could not be identified as purely piston-like or rocking. Yet, the rocking components never exceeded the piston component. Also the 3D motion of the model outcome showed that columellar motions at higher frequencies were too complicated to be identified as purely piston-like or rocking, which was also observed for the reported measurements of stapedial motion in mammals. In the human temporal bone measurements of Hato et al. (2003), rocking-to-piston ratios were also larger with intact IE than with drained IE for most frequencies. With intact IE, however, rotational motions of the footplate exceeded the piston-like motion at 4 kHz and higher, indicating a predominantly rocking motion.

Ideally, CFP motions under intact IE conditions are better addressed through measurement than by a model that makes assumptions about boundary conditions and isotropy and homogeneity of tissues. However, when we compare our model of the ostrich to measurements in human, we observe that the IE influences footplate motions in a similar way, which suggests that the model result is reliable to a certain extent. Nevertheless, to determine what lies at the origin of the observed motions, and how material properties, geometry and boundary conditions of the different ME structures contribute to this motion, sensitivity analyses should be performed in combination with FE modeling.

From the experiments and the model, it can be concluded that the CFP performs largely piston-like motions for sound pressures at low and mid frequencies, where the displacements are not yet too complicated. This implies that the description of rocking motion provided by Gaudin (1968) does at least not apply in the ostrich. When analyzing the piston-like motion of the CFP in the model, it seems that the situation in the ostrich is more complicated than the explanations provided by Pohlman (1921), Norberg (1978) or Manley (1990): in the presented model, the deformable extracolumella and flexible joint convert the existing rotations of the extrastapedial process partially into piston-like motion of the columella. This conversion goes along with bending of the extracolumella and relative rotation at the joint, and the contribution of the joint is the largest. However, piston-like CFP motion is also observed when the extracolumella and joint are considered non-deformable: for instance, when the columella, extracolumella and their connection are modeled as completely bony, the extrastapedial process produces mostly translations that also lead to a piston-like CFP motion without any conversion by bending. However, with a bony extracolumella the displacements of the extrastapedial tip and CFP become too small in magnitude compared to what is observed experimentally. This observation suggests that flexibility of the joint and extracolumella is needed to produce large enough CFP motion rather than to provide piston-like CFP motion, because the latter can also be demonstrated with non-deformable middle-ear components. Yet, further experimental and modeling analysis of the ME structures is needed to make a more conclusive statement.

5. Conclusion

When static pressures of +1 and −1 kPa were applied to the ME of the ostrich, both piston-like and rocking motion was observed at the CFP. In most cases, the rocking-to-piston ratio was larger for negative than for positive ME pressure. For positive ME pressure, the motion was predominantly piston-like. For negative ME pressure, the piston component was mostly larger than the rocking component, but the difference was smaller; in one specimen, rocking motion was even dominant. For the dynamic pressure experiments with frequencies ranging from 0.125 to 4 kHz, the rocking components arising from rotations around the long and short axis of the CFP were mostly much smaller than the piston component. At frequencies below 1 kHz, rocking-to-piston ratios were constant as a function of frequency with values of less than 0.1. For higher frequencies, the rocking components increased relative to the piston component as a function of frequency, although never exceeding the piston component. The IE load affected CFP motions of the model in such a way that the rocking-to-piston ratio increased relative to the condition with unloaded CFP above 0.8 kHz. At higher frequencies, columellar motions could no longer be identified as purely piston-like or rocking.

Conflicts of interest

none.

Contributors

P.G.G.M. carried out the quasi-static and dynamic experiments, constructed the FE model, collected and analyzed the data and wrote the manuscript; R.C. carried out the quasi-static experiments and prepared the specimens; P.A. participated in the design of the study; J.J.J.D. participated in the design of the study, carried out the dynamic experiments and prepared the specimens. All authors gave final approval for publication.

Acknowledgments

The first author has a PhD Fellowship of the Research Foundation of Flanders (FWO). The FWO funded this work, grant numbers 11T9316N and G049414N. We want to thank William Deblauwe, Fred Wiese, Daniël De Greef, Manuel Dierick and Iván Josipovic for their technical assistance.

References

Allen, J.B., 1986. Measurement of eardrum acoustic impedance. In: Allen, J.B., Hall, J.L., Hubbard, A.E., Neely, S.T., Tubis, A. (Eds.), Peripheral Auditory Mechanisms. Springer-Verlag, Berlin, Heidelberg, pp. 44–51. https://doi.org/10.1007/978-3-642-50038-1_6.

Arechvo, I., Zahnert, T., Bornitz, M., Neudert, M., Lasurashvili, N., Simkunaite-Rizgeliene, R., 2013. The ostrich middle ear for developing an ideal ossicular replacement prosthesis. Eur. Arch. Otorhinolaryngol. 270, 37–44. https://doi.org/10.1007/s00405-011-1907-1.

Buytaert, J.A.N., Goyens, J., De Greef, D., Aerts, P., Dirckx, J.J.J., 2014. Volume shrinkage of bone, brain and muscle tissue in sample preparation of micro-CT and light sheet fluorescence microscopy (LSFM). Microsc. Microanal. 20, 1208–1217. https://doi.org/10.1017/S1431927614001329.

Cheng, J.T., Aarnisalo, A.A., Harrington, E., del Socorro Hernandez-Montes, M., Furlong, C., Merchant, S.N., Rosowski, J.J., 2010. Motion of the surface of the human tympanic membrane measured with stroboscopic holography. Hear. Res. 263, 66–77. https://doi.org/10.1016/j.heares.2009.12.024.

Cheng, J.T., Hamade, M., Merchant, S.N., Rosowski, J.J., 2013. Wave motion on the surface of the human tympanic membrane: holographic measurement and modeling analysis. J. Acoust. Soc. Am. 133, 918–937. https://doi.org/10.1121/1.4773263.

Decraemer, W.F., Khanna, S.M., Funnell, W.R.J., 2000. Measurement and modeling of the three-dimensional vibration of the stapes in cat. In: Wada, H., Takasaka, K., Ikeda, K., Phyama, K., Koike, T. (Eds.), Proceeding of the Symposium on Recent Developments in Auditory Mechanics. World Scientific Press, Singapore, pp. 36–43. https://doi.org/10.1142/9789812793980_0006.

Decraemer, W.F., de La Rochefoucauld, O., Dong, W., Khanna, S.M., Dirckx, J.J., Olson, E.S., 2007. Scala vestibuli pressure and three-dimensional stapes velocity measured in direct succession in gerbil. J. Acoust. Soc. Am. 121, 2774–2791. https://doi.org/10.1121/1.2709843.

De Greef, D., Soons, J.A.M., Dirckx, J.J.J., 2014a. Digital stroboscopic holography setup for deformation measurement at both quasi-static and acoustic frequencies. Int. J. Optomechatroni. 8, 275–291. https://doi.org/10.1080/15599612.2014.942928.

De Greef, D., Aernouts, J., Aerts, J., Cheng, J.T., Horwitz, R., Rosowski, J.J., Dirckx, J.J.J., 2014b. Viscoelastic properties of the human tympanic membrane studied with

stroboscopic holography and finite element modeling. Hear. Res. 312, 69–80. https://doi.org/10.1016/j.heares.2014.03.002.
De Greef, D., Pires, F., Dirckx, J.J.J., 2017. Effects of model definitions and parameter values in finite element modeling of human middle ear mechanics. Hear. Res. 344, 195–206. https://doi.org/10.1016/j.heares.2016.11.011.
de La Rochefoucauld, O., Decraemer, W.F., Khanna, S.M., Olson, E.S., 2008. Simultaneous measurements of ossicular velocity and intracochlear pressure leading to the cochlear input impedance in gerbil. JARO 9, 161–177. https://doi.org/10.1007/s10162-008-0115-1.
Edom, E., Obrist, D., Henninger, R., Kleiser, L., Sim, J.H., Huber, A.M., 2013. The effect of rocking stapes motions on the cochlear fluid flow and on the basilar membrane motion. J. Acoust. Soc. Am. 134, 3749–3758. https://doi.org/10.1121/1.4824159.
Eiber, A., Breuninger, C., Sequeira, D., Huber, A., 2007. Mechanical excitation of complex stapes motion in Guinea pigs. In: Huber, A., Eiber, A. (Eds.), Middle Ear Mechanics in Research and Otology. World Scientific Press, Singapore, pp. 123–129. https://doi.org/10.1142/9789812708694_0016.
Eiber, A., Huber, A.M., Lauxmann, M., Chatzimichalis, M., Sequeira, D., Sim, J.H., 2012. Contribution of complex stapes motion to cochlea activation. Hear. Res. 284, 82–92. https://doi.org/10.1016/j.heares.2011.11.008.
Frank, G.H., Smit, A.L., 1976. The morphogenesis of the avian columella auris with special reference to *Struthio camelus*. Afr. Zool. 11, 159–182. https://doi.org/10.1080/00445096.1976.11447522.
Gaudin, E.P., 1968. On the middle ear of birds. Acta Otolaryngol. 65, 316–326. https://doi.org/10.3109/00016486809120971.
Guinan, J.J., Peake, W.T., 1967. Middle-ear characteristics of anesthetized cats. J. Acoust. Soc. Am. 41, 1237–1261. https://doi.org/10.1121/1.1910465.
Gummer, A.W., Smolders, J.W.T., Klinke, R., 1989a. Mechanics of a single-ossicle ear: I. The extra-stapedius of the pigeon. Hear. Res. 39, 1–14. https://doi.org/10.1016/0378-5955(89)90077-4.
Gummer, A.W., Smolders, J.W.T., Klinke, R., 1989b. Mechanics of a single-ossicle ear: II. The columella footplate of the pigeon. Hear. Res. 39, 15–25. https://doi.org/10.1016/0378-5955(89)90078-6.
Hato, N., Stenfelt, S., Goode, R.L., 2003. Three-dimensional stapes footplate motion in human temporal bones. Audiol. Neurotol. 8, 140–152. https://doi.org/10.1159/000069475.
Heiland, K.E., Goode, R.L., Asai, M., Huber, A.M., 1999. A human temporal bone study of stapes footplate movement. Am. J. Otol. 20, 81–86. https://doi.org/10.5167/uzh-8371.
Herrmann, G., Liebowitz, H., 1972. Mechanics of bone fracture. In: Liebowitz, H. (Ed.), Fracture of Nonmetals and Composits. Academic Press, New York, pp. 771–840. https://doi.org/10.1016/b978-0-12-449707-8.50014-2.
Huber, A.M., Linder, T., Ferrazzini, M., Schmid, S., Dillier, N., Stoeckli, S., Fisch, U., 2001. Intraoperative assessment of stapes movement. Ann. Otol. Rhinol. Laryngol. 110, 31–35. https://doi.org/10.1177/000348940111000106.
Huber, A.M., Sequeira, D., Breuninger, C., Eiber, A., 2008. The effect of complex stapes motion on response of the cochlea. Otol. Neurotol. 29, 1187–1192. https://doi.org/10.1097/mao.0b013e31817ef49b.
Khaleghi, M., Lu, W., Dobrev, I., Cheng, J.T., Furlong, C., Rosowski, J.J., 2013. Digital holographic measurements of shape and three-dimensional sound-induced displacements of tympanic membrane. Opt. Eng. 52, 101916. https://doi.org/10.1117/1.OE.52.10.101916.
Kirikae, J., 1960. The Structure and Function of the Middle Ear. University of Tokyo Press, Tokyo.
Larsen, O.N., Christensen-Dalsgaard, J., Jensen, K.K., 2016. Role of intracranial cavities in avian directional hearing. Biol. Cybern. 110, 319–331. https://doi.org/10.1007/s00422-016-0688-4.
Lynch 3rd, T.J., Nedzelnitsky, V., Peake, W.T., 1982. Input impedance of the cochlea in cat. J. Acoust. Soc. Am. 72, 108–130. https://doi.org/10.1121/1.387995.
Maftoon, N., Funnell, W.R.J., Daniel, S.J., Decraemer, W.F., 2015. Finite-element modelling of the response of the gerbil middle ear to sound. JARO 16, 547–567. https://doi.org/10.1007/s10162-015-0531-y.
Manley, G.A., 1990. Overview and outlook. In: Manley, G.A. (Ed.), Peripheral Hearing Mechanisms in Reptiles and Birds. Zoophysiology. Springer-Verlag, Berlin, Heidelberg, pp. 253–273. https://doi.org/10.1007/978-3-642-83615-2_14.
Manley, G.A., Köppl, C., Yates, G.K., 1997. Activity of primary auditory neurons in the cochlear ganglion of the emu Dromaius novaehollandiae: spontaneous discharge, frequency tuning, and phase locking. J. Acoust. Soc. Am. 101, 1560–1573. https://doi.org/10.1121/1.418273.
Masschaele, B., Dierick, M., Van Loo, D., Boone, M.N., Brabant, L., Pauwels, E., Cnudde, V., Van Hoorebeke, L., 2013. HECTOR: a 240 kV micro-CT setup optimized for research. J. Phys. Conf. Ser. 463, 012012, https://doi.org/10.1088/1742-6596/463/1/012012.
Mills, R., Zhang, J., 2006. Applied comparative physiology of the avian middle ear: the effect of static pressure changes in columellar ears. J. Laryngol. Otol. 120, 1005–1007. https://doi.org/10.1017/S0022215106002581.
Mills, R., Zadrozniak, M., Jie, Z., 2007. Ossicular motion during changes in static pressure in the avian middle ear. In: Huber, A.M., Eiber, A. (Eds.), Middle Ear Mechanics in Research and Otology. Proceedings of the 4th International Symposium. World Scientific Publishing, Singapore, pp. 21–25.
Muyshondt, P.G.G., Soons, J.A.M., De Greef, D., Pires, F., Aerts, P., Dirckx, J.J.J., 2016a. A single-ossicle ear: acoustic response and mechanical properties measured in duck. Hear. Res. 340, 35–42. https://doi.org/10.1016/j.heares.2015.12.020.
Muyshondt, P.G.G., Aerts, P., Dirckx, J.J.J., 2016b. Acoustic input impedance of the avian inner ear measured in ostrich (*Struthio camelus*). Hear. Res. 339, 175–183. https://doi.org/10.1016/j.heares.2016.07.009.
Norberg, R.Å., 1978. Skull asymmetry, ear structure and function, and auditory localization in Tengmalm's owl, Aegolius funereus (Linné). Phil. Trans. R. Soc. B 282, 325–410. https://doi.org/10.1098/rstb.1978.0014.
Pohlman, A.G., 1921. The position and functional interpretation of the elastic ligaments in the middle-ear of Gallus. J. Morphol. 35, 228–262. https://doi.org/10.1002/jmor.1050350106.
Ravicz, M.E., Merchant, S.N., Rosowski, J.J., 2000. Effect of freezing and thawing on stapes-cochlear input impedance in human temporal bones. Hear. Res. 150, 215–224. https://doi.org/10.1016/S0378-5955(00)00200-8.
Ravicz, M.E., Cooper, N.P., Rosowski, J.J., 2008. Gerbil middle-ear sound transmission from 100 Hz to 60 kHz. J. Acoust. Soc. Am. 124, 363–380. https://doi.org/10.1121/1.2932061.
Rosowski, J.J., Peake, W.T., Lynch 3rd, T.J., Leong, R., Weiss, T.F., 1985. A model for signal transmission in an ear having hair cells with free-standing stereocilia. II. Macro-mechanical stage. Hear. Res. 20, 139–155. https://doi.org/10.1016/0378-5955(85)90165-0.
Saiff, E.I., 1981. The middle ear of the skull of birds: the ostrich, *Struthio camelus* L. Zool. J. Linn. Soc. 73, 201–212. https://doi.org/10.1111/j.1096-3642.1981.tb01593.x.
Saunders, J.C., Johnstone, B.M., 1972. A comparative analysis of middle-ear function in non-mammalian vertebrates. Acta Otolaryngol. 73, 353–361. https://doi.org/10.3109/00016487209138952.
Starck, J.M., 1995. Comparative anatomy of the external and middle ear of palaeognathous birds. Adv. Anat. Embryol. Cell Biol. 131, 1–137. https://doi.org/10.1007/978-3-642-79592-3.
Sim, J.H., Chatzimichalis, M., Lauxmann, M., Röösli, C., Eiber, A., Huber, A.M., 2010. Complex stapes motions in human ears. JARO 11, 329–341. https://doi.org/10.1007/s10162-010-0207-6.
Thomassen, H.A., Gea, S., Maas, S., Bout, R.G., Dirckx, J.J.J., Decraemer, W.H., Povel, G.D.E., 2007. Do Swiftlets have an ear for echolocation? The functional morphology of Swiftlet's middle ears. Hear. Res. 225, 25–37. https://doi.org/10.1016/j.heares.2006.11.013.
Vallejo Valdezate, L.A., Gil-Carcedo Sañudo, E., Gil-Carcedo Sañudo, M.D., Pablos López, M., Gil-Carcedo García, L.M., 2007. The avian middle ear (*Struthio camelus*). Data for the physiology of sound transmission in systems with a single ossicle in the chain. Acta Otorrinolaringol. Esp. 58, 246–251. https://doi.org/10.1016/s2173-5735(07)70343-5.
Van der Jeught, S., Dirckx, J.J.J., Aerts, J.R.M., Bradu, A., Podoleanu, A.G., Buytaert, J.A.N., 2013. Full-field thickness distribution of human tympanic membrane obtained with optical coherence tomography. JARO 14, 483–494. https://doi.org/10.1007/s10162-013-0394-z.
Volandri, G., Di Puccio, F., Forte, P., Carmignani, C., 2011. Biomechanics of the tympanic membrane. J. Biomech. 44, 1219–1236. https://doi.org/10.1016/j.jbiomech.2010.12.023.
von Békésy, G., 1960. Experiments in Hearing. McGraw-Hill, New York.
Zhang, X., Gan, R.Z., 2011. Experimental measurement and modeling analysis on mechanical properties of incudostapedial joint. Biomech. Model. Mechanobiol. 10, 713–726. https://doi.org/10.1007/s10237-010-0268-9.